Parallel full-wave electromagnetic field analysis based on hierarchical domain decomposition method

Amane Takei*
Faculty of Engineering, University of Miyazaki,1-1, Gakuen Kibanadai-Nishi Miyazaki, 889-2192, Japan

Nanako Mizoguchi
Faculty of Engineering, University of Miyazaki,1-1, Gakuen Kibanadai-Nishi Miyazaki, 889-2192, Japan

Kento Ohnaka
Graduate School of Engineering, University of Miyazaki,1-1, Gakuen Kibanadai-Nishi Miyazaki, 889-2192, Japan

Makoto Sakamoto
Faculty of Engineering, University of Miyazaki,1-1, Gakuen Kibanadai-Nishi Miyazaki, 889-2192, Japan

**Corresponding Author*

E-mail:takei@cc.miyazaki-u.ac.jp
http://www.miyazaki-u.ac.jp/

Abstract

In this presentation, a parallel full-wave electromagnetic field analysis code based on an iterative domain decomposition method is explained that is named ADVENTURE_Fullwave. A stationary vector wave equation for the high-frequency electromagnetic field analyses is solved taking an electric field as an unknown function. Then, to solve subdomain problems by the direct method, the direct method based on the LDL^T decomposition method is introduced in subdomains. The simplified Berenger's PML is introduced which these eight corners are given the average value of all PML's layers. And, we show a numerical example of a microwave. More detail will be shown in the conference.

Keywords: Electromagnetic field analysis, Finite element method, Domain decomposition method, Huge-scale analysis.

1. Introduction

Electromagnetic field analysis based on a numerical analysis method, such as the finite element method, has become widespread [1] due to recent improvements in computer performance and numerical calculation technology. In the case of accurately reproducing an analysis model of complicated shape, it is necessary to use many small the elements. In the case of analyzing the state of electromagnetic waves propagation in a wide range, a wide analysis domain is examined. Furthermore, to perform a high-accuracy analysis, it is necessary to model the analysis domain with a sufficiently small element for the wave-length, and, in this case, the number of elements also increases. Increasing the number of elements increases the scale of the problem. Therefore, a method that can calculate large-scale problems has come to be demanded. Moreover, large-scale problems must be solved with high accuracy. In the presentation, a large-scale analysis code: ADVENTURE_Fullwave is introduced, and detail of the parallel algorism is shown.

2. Governing equations and algorithm for parallel computing

In ADVENTURE_Fullwave, the full-wave analysis based on an E method [1] is considered. $\mathbf{E}_{\mathrm{h}}$ and $\mathbf{J}_h$ are finite element approximations of electric field $\mathbf{E}$ [V/m] and current density $\mathbf{J}$ [A/m^2], respectively. The permeability is given by $\mu = \mu_0\mu_r$ [H/m], μ_0 is the vacuum permeability [H/m], and μ_r is the relative permeability. The complex permittivity is given by $\varepsilon = \varepsilon_0\varepsilon_r - \sigma/j\omega$ [F/m], ε_0 is the vacuum permittivity [F/m], ε_r is the relative permittivity, and ω is the angular frequency [rad/s]. The following equation is the finite element equation to be solved:

$$\iiint_{\Omega} (1/\mu)\mathrm{rot}\mathbf{E}_{\mathrm{h}} \cdot rot\mathbf{E}_{\mathrm{h}}{}^{*} dv - \omega^2 \iiint_{\Omega} \varepsilon\mathbf{E}_{\mathrm{h}} \cdot \mathbf{E}_{\mathrm{h}}{}^{*} dv = j\omega \iiint_{\Omega} \mathbf{J}_h \cdot \mathbf{E}_h{}^{*} dv. \quad (1)$$

The equation contains complex numbers and becomes a complex symmetric matrix. In the present study, the electric field $\mathbf{E}$, which is unknown, is obtained using the conjugate orthogonal conjugate gradient (COCG) method. The finite element approximation (1) is rewritten as $Ku = f$ by the coefficient matrix K, the unknown vector u, and the right-hand side vector f. Next, Ω is divided into N subdomains (Eq. (2)). Eq. (3) and (4) are obtained from Eq. (2).

$$\begin{bmatrix} K_{II}^{(1)} & 0 & 0 & K_{IB}^{(1)}R_B^{(1)\mathrm{T}} \\ 0 & \ddots & 0 & \vdots \\ & & K_{II}^{(N)} & K_{IB}^{(N)}R_B^{(N)\mathrm{T}} \\ 0 & 0 & & \\ R_B^{(1)}K_{IB}^{(1)\mathrm{T}} & \cdots & R_B^{(N)}K_{IB}^{(N)\mathrm{T}} & \sum_{i=1}^{\mathrm{N}} R_B^{(i)}K_{BB}^{(i)}R_B^{(i)\mathrm{T}} \end{bmatrix} \begin{bmatrix} u_I^{(1)} \\ \vdots \\ u_I^{(N)} \\ u_B \end{bmatrix} = \begin{bmatrix} f_I^{(1)} \\ \vdots \\ f_I^{(N)} \\ f_B \end{bmatrix} \quad (2)$$

$$K_{II}^{(i)}u_I^{(i)} = f_I^{(i)} - K_{IB}^{(i)}u_B^{(i)} \quad (i = 1, \ldots, N) \quad (3)$$

$$\left\{\sum_{i=1}^{\mathrm{N}} R_B^{(i)}\left\{K_{BB}^{(i)} - K_{IB}^{(i)\mathrm{T}}\left(K_{II}^{(i)}\right)^{-1}K_{IB}^{(i)}\right\}R_B^{(i)T}\right\}u_B = \sum_{i=1}^{\mathrm{N}} R_B^{(i)}\left\{f_B^{(i)} - K_{IB}^{(i)T}\left(K_{II}^{(i)}\right)^{-1}f_I^{(i)}\right\} \quad (4)$$

where $f_B{}^{(i)}$ is the right-hand vector for u_B, and $\left(K_{II}^{(i)}\right)^{-1}$ is the inverse matrix of $K_{II}^{(i)}$. Equation (4) is referred to as an interface problem and is an equation for satisfying the continuity between domains in the domain decomposition method. For simplicity, rewrite Eq. (5) as follows:

$$Su_B = g,$$
$$S = \sum_{i=1}^{N} R_B^{(i)}S^{(i)}R_B^{(i)T}, \quad S^{(i)} = K_{BB}^{(i)} - K_{IB}^{(i)T}\left(K_{II}^{(i)}\right)^{-1}K_{IB}^{(i)}. \quad (5)$$

3. PML

3.1. *Berenger's PML*

The PML can be used to create an absorbing boundary by surrounding the analysis domain with a PML. From the viewpoint of the accuracy of the obtained solution, the PML is currently the most effective absorbing boundary condition. Although Berenger's PML is originally proposed as an absorbing boundary condition for the FDTD method, in the present study, we apply a finite element method dealing with an unstructured grid, we propose a simplified method omitting the directionality of electric conductivity given to the PML and confirm its effectiveness.

Berenger's PML [2] stacks several PMLs outside the analysis domain and gradually sets a large value of electric conductivity according to the outer layer so that the outermost wall can be surrounded with a perfect conductor wall without reflecting electromagnetic waves. Figure 1 shows a schematic diagram of Berenger's PML absorbing boundary.

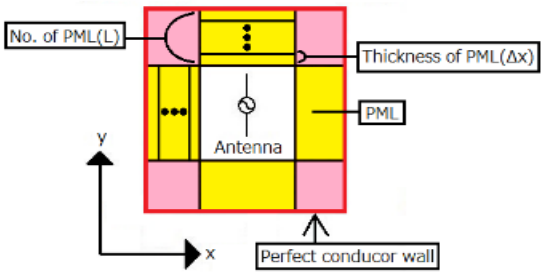

Fig. 1. PML absorbing boundary

In this paper the distribution of the electric conductivity for PML is expressed as follows:

$$\sigma = \sigma_{max}\left[\frac{\left(L - \hat{L}(x)\right)\Delta x}{L\Delta x}\right]^{M} \quad (6)$$

where Δx is the thickness of PML 1, L is the number of layers of the PML, $\hat{L}(x)$ is a coefficient determined by position x, and $\hat{L}(x)$ = 0 at the position of the Lth layer,

$\hat{L}(x)$ = 1 at the position of the (*L-1*)th layer, and $\hat{L}(x)$ = *L* -1 at the position of the first layer.
Moreover, σ_{max} is the maximum value of the electric conductivity for the PML, and *M* is the degree distribution of electric conductivity. This equation is used to determine the electric conductivity of each layer of the PML.

The parameters to be determined as the parameters of the PML are the thickness Δx of PML 1, the number L of PML layers, the maximum electric conductivity σ_{max} of the PML, the degree *M* distribution of the electric conductivity, the reflection coefficient *R* [dB] between the PML of the outermost layer, and the perfect conductor wall. The reflection coefficient *R* is approximated as follows:

$$|R(\phi)| \cong exp\left[-\frac{2\sigma_{max}L\Delta x}{(M+1)\varepsilon_0 c}\cos\phi\right] \quad (7)$$

where ϕ is the incident angle of the electromagnetic wave, and c is the speed of light. Since we cannot decide the incident angle for an arbitrary incident wave, ϕ = 0, a reflection coefficient for perpendicular incidence is used as a reference. Moreover, since the *M* that gives the distribution of the electric conductivity causes the calculation accuracy to deteriorate if the change of the electric field in the PML is too steep, *M* is approximately 2 to 4. If the number of layers L is too large, more memory will be required, and if *L* is too small, it will not function adequately as an absorbing boundary. There are many cases where the concrete number of *L* is set to 4 to 16. The thickness Δx of PML 1 is a constant thickness of all layers.
We set the reflection coefficient *R*(0) according to the required accuracy. Upon determining the above parameters, the maximum electric conductivity σ_{max} is given as follows:

$$\sigma_{max} = -\frac{(M+1)\varepsilon_0 c}{2L\Delta x}\ln|R(0)| \quad (8)$$

In the present study, we construct a PML using Eq. (6) through Eq. (8) with *L* = 9, *M* = 4, and $\Delta x = \lambda/10$. However, in order to reduce the analysis scale, we examine the optimum value of *L* in the next section.

3.2. *Numerical results*

We assign the PML to the dipole antenna model. The analysis domain is a cube of length 0.6 [m] so that the distance from the antenna to the innermost PML matches the wavelength. The current density is applied to the antenna as a current source as follows:

$$I(y) = I_0\cos\left(\frac{2\pi}{\lambda}y\right) \quad : -l \le y \le l \quad (9)$$

where I_0 = 0.08 [A/m^2], λ is the wavelength, and l is the length from the feeding point to the antenna tip.
The analysis frequency is 1 [GHz], and the length of the antenna is 0.15 [m], which is the half wavelength. Here, mesh division is performed so that the maximum side length of the element is 1/20 of the wavelength. The analysis domain's boundary is a perfect conductor. Figure 4 shows a schematic diagram of the dipole antenna model.

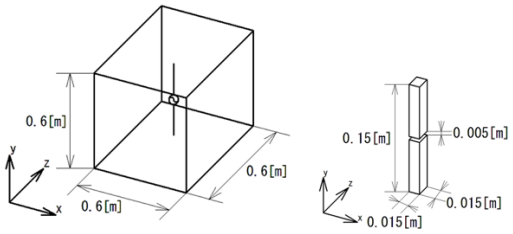

(a) Analysis domain (b) Antenna

Fig. 2. Dipole antenna model

We assign PMLs to the domain boundary as shown in Fig. 2(a). The plane portion of the PML at the domain boundary overlaps a number of flat plates according to the number of layers, and the corner portion of the PML is one rectangular parallelepiped or cube. The boundary of the outermost layer of the PML is a perfect conductor wall. We perform performance evaluation by setting the thickness of one layer to be 0.03 [m] and the PML to have *L* = 9 (hereinafter a PML with *L* layers is abbreviated as PML(*L*)). Table 1 lists the number of elements and the degree of freedom of the analysis model.

Table 1. Number of elements and DOFs of the dipole antenna model

	PML(0): Perfect conductor wall	PML(9)
No. of Elements	4,669,759	26,899,669
DOFs	5,506,368	31,703,550

In (8), we set *L* = 9, Δx = 0.03, *M* = 4, and *R*(0) = -120 [dB], which yields the maximum electric conductivity σ_{max} to PML(9). In addition, we decide the electric conductivity of each layer using (6). In this study, we set the average value of each layer to the electric conductivity of the corner portion. We evaluate the performance of the PML based on the reflection coefficient obtained using the S_{11} parameter[3]. The observation point of the S_{11} parameter is on the x-axis 1

cm inside of the PML. The computing environment in the present study is a 25-PC cluster with Intel Core i7-2600K multi-core CPUs (total: 100 cores) and 32 GB memory. Table 2 lists the reflection coefficient, the CPU time, and the memory size.

Table 2. Results for reflection coefficient, CPU time, and memory size

	PML(0): Perfect conductor wall	PML(9)
Reflection coefficient [dB]	0	-18.65
CPU time [s]	1,278	18,787
Memory size [MB/core]	44.3	227.3

When the domain boundary is PML(0), i.e., when it is a perfect conductor wall, S_{11} = 1, so that the reflection coefficient is 0 [dB]. On the other hand, when the domain boundary is PML(9), the reflection coefficient is -18.65 [dB]. The design target reflection coefficient of the antenna, for example, is generally approximately -10 to -20 [dB], and in the present study, we use a reflection coefficient of approximately -10 to -20 [dB][3]. Thus, PML(9) can obtain sufficient absorption performance. On the other hand, in comparing with PML (0), PML (9) increases the amount of memory used and computation time, depending on the absorbing layer applied. Figure 3 shows a visualization diagram of the electric field obtained by analysis.

In Figure 3, the left-hand side shows PML(9) at the boundary edge and the electric field propagates from the dipole antenna to the free space. On the other hand, the right-hand side of Figure 3 shows the mode when the dipole antenna is enclosed by a perfect conductor wall.

Next, we perform the directivity evaluation of the dipole antenna by error evaluation using the theoretical solution in the far field. The error evaluation of the far field uses the E plane.

The theoretical solution[3] of the far field of the E plane is as follows:

$$E_\theta = j60I\frac{e^{-jkr}}{r}\cdot\frac{\cos\left(\frac{\pi}{2}\cos\theta\right)}{\sin\theta} \tag{10}$$

where j is the imaginary unit, I is the current, and r is the distance from the feeding point. The approximate distance r to the far-field peak of the Fresnel's region ($2\,l^2/\lambda < r$) is 0.250 [m], if the dimension l (= 0.150 [m]) of the dipole antenna is not ignored. Moreover, k is the wave number and is given by $k = 2\pi/\lambda$. The directivity evaluation is performed by comparing the numerical analysis solution with the theoretical solution on the E plane. Figure 4 shows a plot of the numerical analysis solution e_θ and the theoretical solution E_θ in increments of 1 [deg].

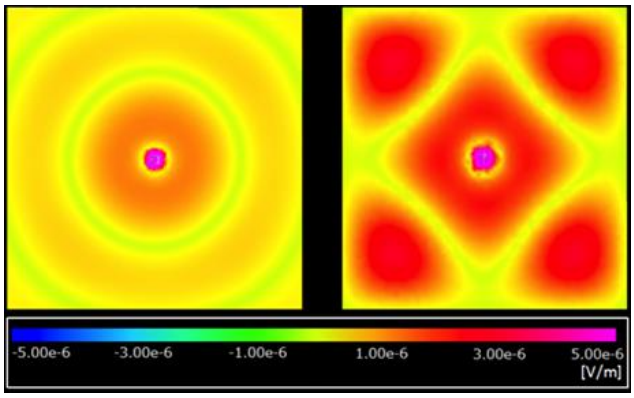

Fig. 3. **V**isualization of the analysis result (electric field) (Left: PML(9), Right: PML(0) (perfect conductor wall))

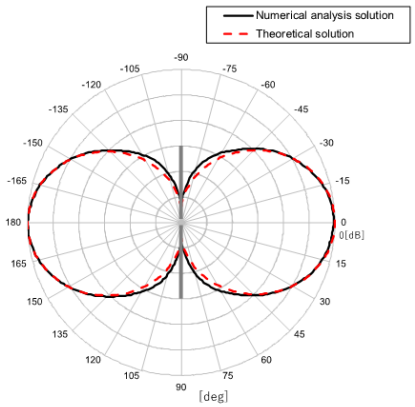

Fig. 4. Numerical and theoretical solutions in the E plane

The directivities of the numerical and theoretical solutions agree very well. The range of θ, which is the far field far beyond the Fresnel's region, can be expressed by (11). The lower limit θ_{Min} is $\arcsin(2\,l^2/r\lambda) + 90 \cong -57$ [deg], and the upper limit θ_{Max} is $90 - \arcsin(2\,l^2/r\lambda) \cong 53$ [deg]. The average error rate E_{err} in this range is obtained by (12). As a result, the average error rate is 1.70 [%], and it is shown that a highly accurate solution can be obtained.

$$\arcsin\left(\frac{2\,l^2}{r\lambda}\right) + 90 \le \theta \le 90 - \arcsin\left(\frac{2\,l^2}{r\lambda}\right) \tag{11}$$

$$E_{err} = \frac{\sum_{i=\theta_{Min}}^{\theta_{Max}} \frac{|e_i - E_i|}{E_i}}{\theta_{Max} - \theta_{Min} + 1} \times 100 \quad [\%] \tag{12}$$

In the calculations shown in Figure 2, we used a dipole antenna model with PML(9). Here, we find the optimum L from the average error rate in the far field and the reflection coefficient of PML(L) by a parameter study using the number of PMLs. Table 3 shows the number of elements for each L, the number of degrees of freedom of the edge, the error rate, the reflection coefficient, the calculation time, and the number of iterations of the COCG method applied to the interface problem.

Table 3. Numerical model data and results

	PML(9)	PML(8)	PML(7)
No. of elements	26,899,669	24,184,687	21,533,641
DOFs	31,703,550	28,506,352	25,383,890
Average error rate [%]	1.70	3.81	12.87
Reflection coefficient [dB]	-18.65	-15.79	-15.04
CPU time [h]	5.22	3.77	2.81
No. of iterations	46,508	37,755	30,695
Memory size [MB/core]	227.3	204.6	182.6

From Table 3, PML(9) is the case with the best far field accuracy. When the allowable range of the error rate is less than 5 [%], which is the allowable range of numerical analysis error, since PML(7) has a reflection coefficient of less than -15 [dB], the PML functions sufficiently. However, the error rate exceeded the allowable range. We can find that PML(8) is optimal because it has a better calculation time and iteration count than PML(9).

4. Analysis for Convergence Comparison

4.1. *Results of Closed-space model A*

The number of iterations and computation time for the closed-space model A with subdomain sizes of 100, 200, 500, and 1,000 are shown in Table 4. The convergence decision value is 1.0e-03. As shown in Figure 5, the convergence performance improves as the size of the subdomain increases.

Table 4. Result of closed-space model A(2,549,500 Elemens.)

Subdomain size	Num of iterations	Computation time [sec]
100	10,459	453
200	9,202	414
500	6,847	342
1,000	4,848	294

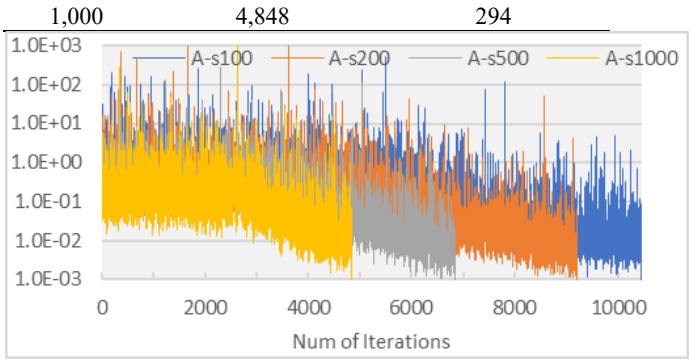

Fig. 5. The num. of iterations and Convergence in model A

4.2. *Results of liberated-space model B*

The number of iterations and computation time for the liberated-space model B with subdomain sizes of 100, 200, 500, 1000, 2000, 5000, and 10000 are shown in Table 5. The convergence decision value is 1.0e-03. As shown in Figure 6, the convergence performance improves as the size of the subdomain increases. More details will be shown at the conference.

Table 5. Result of closed-space model B(15,712,684 Elemens.)

Subdomain size	Num of iterations	Computation time [sec]
100	6,578	1,039
200	10,130	1,636
500	3,581	712
1,000	5,324	1,385
2,000	2,916	1,141
5,000	5,854	3,627
10,000	1,002	973

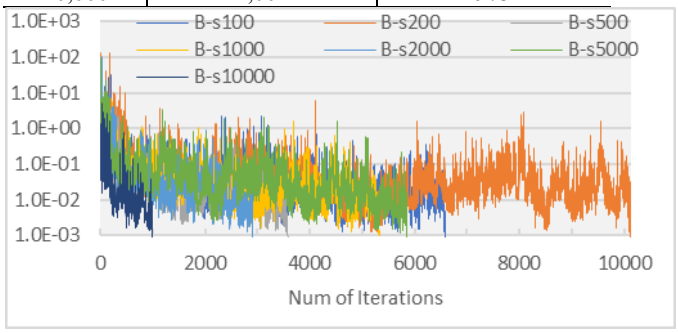

Fig. 6. The num of iterations and Convergence in model B

Acknowledgements

The present study was supported in part by a JSPS Grant-in-Aid for Scientific Research (Basic Research (B), 17H03256). The computer environment used in the

present study was supported in part through a JST Adaptable and Seamless Technology transfer Program (A-STEP (Search Type), AS262Z02631H).

References

1. A. Takei, S. Sugimoto, M. Ogino, S. Yoshimura, H. Kanayama: Full Wave Analyses of Electromagnetic Fields with an Iterative Domain Decomposition Methodm, IEEE Transactions on Magnetics, 46:8 (2010), 2860-2863.
2. A. Takei, I. Higashi, M. Aikawa and T. Yamada, "Microwave analysis based on parallel finite element method," Journal of Advanced Simulation in Science and Engineering, 6:1 (2019), 215-233.

Authors Introduction

Prof. Amane Takei

Amane Takei is working as Associate Professor for Department of Electrical and systems Engineering, University of Miyazaki, Japan. His research interest includes high performance computing for computational electromagnetism, iterative methods for the solution of sparse linear systems, domain decomposition methods for large-scale problems. Prof. Takei is a member of IEEE, an expert advisor of The Institute of Electronics, Information and Communication Engineers (IEICE), a delegate of the Kyushu branch of Institute of Electrical Engineers of Japan (IEEJ), a director of Japan Society for Simulation Technology (JSST).

Ms. Nanako Mizoguchi

She received her B.S. degree in Engineering in 2023 from the Faculty of Engineering, University of Miyazaki in Japan. She is a master course student of Graduate school of Engnnering, University of Miyazaki in Japan.

Mr. Kento Ohnaka

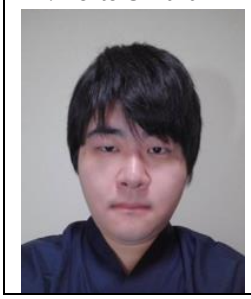

He received his B.S. degree in Engineering in 2022 from the Faculty of Engineering, University of Miyazaki in Japan. He is a master course student of Graduate school of Engnnering, University of Miyazaki in Japan.

Prof. Makoto Sakamoto

Makoto Sakamoto received the Ph.D. degree in computer science and systems engineering from Yamaguchi University. He is presently an associate professor in the Faculty of Engineering, University of Miyazaki. He is a theoretical computer scientist, and his current main research interests are automata theory, languages and computation. He is also interested in digital geometry, digital image processing, computer vision, computer graphics, virtual reality, augmented reality, entertainment computing, complex systems and so on.